Plasma Phys. Control. Fusion **50** (2008) 124041 (17pp) doi:10.1088/0741-3335/50/12/124041

Physics, simulation and diagnostics of Hall effect thrusters

J C Adam[1], J P Boeuf[2], N Dubuit[1,2], M Dudeck[3], L Garrigues[2], D Gresillon[4], A Heron[1], G J M Hagelaar[2], V Kulaev[3], N Lemoine[5], S Mazouffre[3], J Perez Luna[2], V Pisarev[4], S Tsikata[4]

[1] CPHT, CNRS, Ecole Polytechnique, 91128 Palaiseau, France
[2] LAPLACE, CNRS, Université of Toulouse, 118 route de Narbonne, 31062 Toulouse, France
[3] ICARE, CNRS, 1c Av. de la Recherche Scientifique, 45071 Orléans, France
[4] LPTP, CNRS, Ecole Polytechnique, 91128 Palaiseau, France
[5] LPMIA, CNRS, Université Henri Poincaré, Nancy, France

E-mail: jpb@laplace.univ-tlse.fr

Received 1 June 2008, in final form 26 August 2008
Published 5 November 2008
Online at stacks.iop.org/PPCF/50/124041

Abstract

This paper presents recent efforts to better understand and quantify charged particle transport in Hall effect thrusters (HETs). Particle-in-cell (PIC) models, hybrid models, laser induced fluorescence (LIF) measurements and collective scattering (CS) experiments are combined to get a better insight into anomalous electron transport in HETs and to increase the predictive capabilities of simulation codes.

PIC models have demonstrated that plasma turbulence associated with the development of a high frequency, short wavelength azimuthal instability can be responsible for anomalous transport. Scaling laws for anomalous electron mobility have not yet been derived and hybrid models, which are more practical than PIC models for parametric studies, must use empirical, adjustable transport coefficients that can be inferred from PIC results or LIF measurements of the ion velocity distribution function. CS experiments are aimed at validating the PIC model predictions of the azimuthal instability. The CS results show the first direct experimental evidence of the azimuthal instability predicted by the PIC code. The paper illustrates the synergy between experiments and models toward a complete and quantitative understanding of the physics of HETs.

(Some figures in this article are in colour only in the electronic version)

1. Introduction—electric propulsion and Hall effect thrusters (HETs)

1.1. Electric propulsion

Electric propulsion makes use of electrical power to accelerate a propellant. The propellant in electric thrusters (charged particles) can be accelerated to velocities up to twenty times larger than those of chemical thrusters. The higher exhaust velocity of electric thrusters reduces the mass needed to provide a given impulse leading to reduction in launch mass and substantial cost savings. A given space mission is characterized by the total impulse provided to the space vehicle or by its total velocity increment. Integrating the total momentum conservation of the satellite assuming a constant exhaust velocity v_e of the propellant, the total velocity increment Δv of the vehicle between times 0 and t can be written, as a first approximation, as $\Delta v = v_e \ln(m_0/m_t)$, where m_0 is the vehicle mass at the beginning of the thrust period, m_t is its mass at the end of the thrust period. The mass consumption $\Delta m = m_0 - m_t$ at time t is therefore:

$$\Delta m = m_0 \left[1 - \exp\left(-\frac{\Delta v}{v_e} \right) \right]. \tag{1}$$

From this equation it is clear that larger exhaust velocities lead to smaller mass consumption. For example, a total velocity increment of $\Delta v = 750\,\mathrm{m\,s^{-1}}$ is typically needed to maintain a 3 ton satellite on a geostationary orbit for 15 years. Using an electric thruster with an exhaust velocity of $20\,\mathrm{km\,s^{-1}}$ would lead to a propellant mass consumption of about 100 kg, while nearly 1000 kg would be required for a chemical thruster with an exhaust velocity of $2\,\mathrm{km\,s^{-1}}$. On the other hand, the thrust generated by electric thrusters is limited because of the limited available electric power, but the total energy available is not limited (energy from solar cells). Electric thrusters are therefore well suited for low thrust, high velocity increment, long duration applications such as [1]:

- Geostationary Earth Orbit communications (station keeping, orbit transfer)
- Low Earth Orbit communication constellations (orbit transfer, drag compensation, orbit and attitude control)
- Interplanetary missions

Electric thrusters are generally classified into three main categories [2], electrothermal, electrostatic and electromagnetic.

1.2. Hall effect thrusters

HETs, which are the subject of this paper, can be classified either in the second or third category. The thrust in Hall thrusters can be viewed as being due to the electrostatic force generated by the plasma electric field acting on the positive ions. In this sense HETs are electrostatic thrusters (they are 'gridless' ion sources). The thrust can also be described as being due to the Lorentz force acting on the Hall current, and in that sense, they can be classed as electromagnetic thrusters.

A schematic representation of a HET is shown in figure 1(*a*). The plasma is formed in the channel between two coaxial dielectric cylinders. The gas (xenon) is injected from the anode, at one end of the channel. The ions are extracted at the other end of the channel (exhaust plane) and the cathode (heated hollow cathode) is outside the channel. A radial magnetic field B_r is generated in the exhaust plane by several coils and a magnetic circuit. The magnetic field is maximum around the exhaust plane (on the order of 2×10^{-2} T) and decreases to smaller values ($\sim 10^{-3}$ T) on length scales of the order of 1 cm (see figure 1(*b*)). The channel

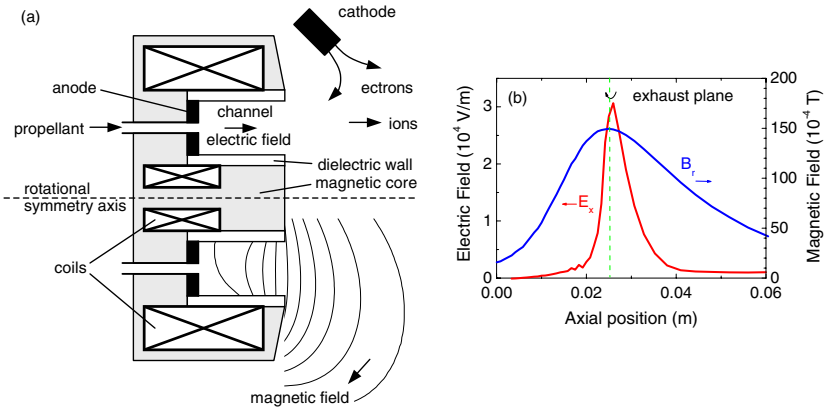

Figure 1. (*a*) Schematic of a HET, (*b*) external radial magnetic field and calculated axial electric field as a function of axial position along a line passing through the middle of the channel. The applied voltage is 300 V, the xenon mass flow rate is 5 mg s^{-1}. The electric field is obtained from a hybrid model and is averaged in time.

length is 2.5 cm and the radii of the concentric cylinders are 3.45 and 5 cm for the PPS®1350[3] thruster of Snecma. Under nominal operating conditions of the PPS®1350, the mass flow rate of the xenon injected at the channel end is 5 mg s^{-1}, the applied voltage is 300 V and the electrical power is 1350 W. The generated thrust under these conditions is 80 mN, and the average exhaust velocity is between 15 and 20 km s^{-1}.

The interesting property of Hall thrusters is that positive ions are extracted from the plasma without grids. The electric field (axial electric field, E_x) is generated in the plasma by the drop in electron conductivity resulting from the presence of an external magnetic field in the direction perpendicular to the electron current from cathode to anode (radial magnetic field, B_r). In this cylindrical $E \times B$ field configuration, an azimuthal ($E \times B$ direction) electron current is generated, the Hall current, which can be about ten times larger than the axial electron current in the acceleration region. The electrons trapped by the radial magnetic field lines oscillate back and forth between the Debye sheaths on the channel walls while rotating in the azimuthal direction with a mean velocity on the order of E_x/B_r. The efficient trapping of electrons by the radial magnetic field increases the residence time of electrons in the exhaust region, leading to practically full ionization of the gas flow which, in turn, decreases the collisional electron transport across B and reinforces electron trapping by the magnetic field. Because of the low neutral density in the acceleration and exhaust region collisional transport across B is not sufficient to explain the experimental results and anomalous electron transport must be invoked. Anomalous transport has been attributed to electron–wall scattering or to field fluctuations. Understanding and quantifying anomalous electron transport is still an issue and a fully self-consistent model able to accurately predict the operating of HETs and to help in designing new thrusters is not yet available.

The ion beam extracted from the plasma is neutralized by part of the electron current emitted by the external cathode. Since the axial electric field is generated in the plasma by the drop in electron conductivity, the extracted ion current density is not space charge limited, as in conventional gridded ion sources (Child–Langmuir law). Therefore, the thrust per unit surface of the extracting region that can be achieved in HETs can be significantly larger than in gridded ion sources.

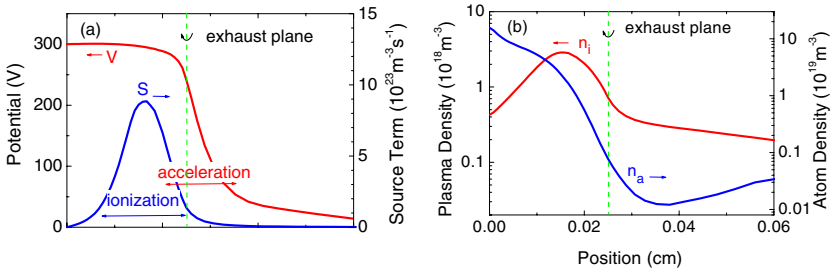

Figure 2. Distributions, along the channel axis of a HET of (*a*), the calculated electric potential, V, and ionization rate, S, (*b*) the plasma density, n_i, and atom density, n_a. The applied voltage is 300 V, the xenon mass flow rate is 5 mg s^{-1}. The results are from a hybrid model and are averaged in time.

More details on the basic properties of HETs and on the history of HET development can be found in Morozov's review papers [4, 5]. The paper by Kim [6] gives useful and simple scaling laws that can be considered for the design of HETs.

1.3. Content of this paper

As mentioned above, the understanding and quantitative description of anomalous electron transport in a HET is still an issue. Further progress toward reliable HET modelling and simulation implies basic research efforts. This paper presents recent efforts of French laboratories aimed at understanding anomalous transport in these devices and at providing modeling tools allowing a self-consistent and sufficiently accurate description of HETs. The aim is to reach a real predictive capability of the simulation codes in order to achieve reliable aided design of HETs. Section 2 presents a short summary of previous work on anomalous electron transport in HETs. Section 3 describes how particle-in-cells (PICs) and hybrid models have been used in conjunction with plasma diagnostics to increase our insight into the physics of HETs. Section 4 focuses on the laser induced fluorescence (LIF) diagnostic used to measure the ion velocity distribution function (VDF), and to get indirect information about the electric field and electron conductivity. Finally section 5 describes recent efforts toward characterizing the plasma fluctuations by collective scattering (CS) experiments.

2. Anomalous electron transport in HETs

The main characteristics of the plasma of a HET are represented in figure 2. For a xenon mass flow rate of $\dot{m} = 5\,\mathrm{mg\,s^{-1}}$, as used in the simulations, full ionization (singly charged ions) of the neutral flow would give an ion current $e\dot{m}/M = 3.7\,\mathrm{A}$, where M is the xenon atom mass. Time averaged plasma density, neutral atom density and ionization rate deduced from a 2D hybrid model (see section 3) are plotted in figure 2 along a line parallel to the thruster axis and at a radial position in the middle of the channel. The neutral atom density is on the order of 10^{19}–$10^{20}\,\mathrm{m^{-3}}$ in the injection region (anode), and drops by two orders of magnitude in the ionization region. 90% or more of the xenon atom flux is ionized. The increase in the atom density in the plasma jet away from the exhaust plane is due to the background pressure of 2 mPa considered in the simulation. The plasma density reaches values of a few $10^{18}\,\mathrm{m^{-3}}$ in the ionization region and decreases as the ions are accelerated in the acceleration region. The axial electric field is concentrated in the region of large magnetic field, where the electron conductivity is the lowest. A large part of the acceleration can take place outside the channel

as seen in figure 2(*a*). The hybrid model results plotted in figure 2 are strongly dependent on the assumptions that are made on the 'anomalous' transport coefficients (see below) and, although this figure represents well the main plasma properties, some details of the space distributions of the plasma properties of figure 2 may be not accurate. These 'details' may however have a strong impact on the operation of the thruster. For example the exact location of the acceleration region with respect to the exhaust plane has a strong impact on the divergence of the ion beam and the sputtering of the ceramic channel wall and can significantly affect the life time of the thruster.

Because of the small atom density, the electron mean free path is much larger than the channel dimensions. The electron–atom collision frequency in xenon is about [7, 8] $\nu_{\text{neutr}} \approx 2.5 \times 10^{-13} n_{\text{a}}$ (n_{a} is the atom density) for a mass flow rate of 5 mg s^{-1}. This gives a collision frequency on the order of $\nu_{\text{neutr,anode}} \approx 10^7$ s^{-1} near the anode, and of less than $\nu_{\text{neutr,exhaust}} \approx 10^5$ s^{-1} in the exhaust region, because of the neutral depletion due to ionization. Assuming classical, collisional conductivity, the electron current density in the axial and azimuthal directions, j_{ex}, and $j_{\text{e}\theta}$, can be written as

$$j_{\text{ex}} = \frac{e^2}{m_{\text{e}}} n_{\text{e}} \frac{\nu_{\text{m}}}{\Omega^2 + \nu_{\text{m}}^2} E_x \approx e n_{\text{e}} \frac{E_x}{B_r} \frac{\nu_{\text{m}}}{\Omega} \qquad \text{and} \qquad j_{\text{e}\theta} = \frac{e^2}{m_{\text{e}}} n_{\text{e}} \frac{\Omega}{\Omega^2 + \nu_{\text{m}}^2} E_x \approx e n_{\text{e}} \frac{E_x}{B_r}. \quad (2)$$

ν_{m} is the total electron momentum transfer frequency, Ω is the electron cyclotron angular frequency and Ω/ν_{m} is the Hall parameter (ratio of the Hall current density to the axial current density). In a HET the Hall parameter is generally much larger than 1 everywhere. The mobility in the axial direction is $\mu_\perp \approx \frac{1}{B_r} \frac{\nu_{\text{m}}}{\Omega}$ and the azimuthal electron drift velocity is $V_{\text{D}} \approx E_x/B_r$ (on the order of 2×10^6 m s^{-1} at the exhaust, see figure 2(*a*)).

The electron cyclotron angular frequency in the exhaust region (typically $B_r \sim 1.5 \times 10^{-2}$ T for a 1 kW thruster) is $\Omega_{\text{exhaust}} \approx 2.6 \times 10^9$ s^{-1}. If electron–atom collisions were the only mechanism responsible for electron transport across the magnetic field, the Hall parameter in the exhaust region would be on the order of or larger than $\Omega_{\text{exhaust}}/\nu_{\text{neutr,exhaust}} \approx 10^4$. This is much larger than what can be inferred from measurements of the Hall and axial currents [6, 8], and leads to an effective axial mobility less than $\mu_\perp \approx 0.007$ m^2 V^{-1} s^{-1} for the above conditions, more than one order of magnitude smaller than the mobility that can be deduced from experiments [8, 10–12]. Two mechanisms can be responsible for anomalous electron transport in the conditions of a HET and have been considered in the literature, (1) scattering of electrons by the wall and secondary electron emission due to electron impact on the wall ('near wall conductivity' [5]) and (2) plasma turbulence ('Bohm-like' conductivity or diffusion).

Recent papers [13–16] have been devoted to the estimation of the contribution of electron–wall collisions to the overall electron conductivity in the channel. These models are generally based on a simple sheath theory (assuming a Maxwellian electron distribution function) including the effect of secondary electron emission and providing an effective collision frequency representing the effect of electron–wall scattering and secondary electron emission [13–15]. Sydorenko *et al* [16] emphasize that the electron VDF is not Maxwellian in a HET and that this has important consequences for the derivation of the electron conductivity due to wall collisions. An exact or satisfying theory of near wall conductivity in a Hall thruster is not yet available.

Fully kinetic models describing self-consistently electron–wall interactions as well as possible turbulence are not available and would involve very time consuming 3D PIC Monte Carlo collisions simulations. The possible role of fluctuations on electron transport in HETs has been recently demonstrated by Adam *et al* [17] using a 2D (axial–azimuthal) PIC model. The PIC simulations show the development of fluctuations of the azimuthal electric

field with wavelength on the order of the electron gyroradius. These fluctuations induce a diffusion across the magnetic field. Many features predicted by the PIC simulations are in good agreement with experimental observations. More detailed results from PIC simulations are presented in the next section.

PIC simulations are not practical for parametric studies in realistic geometry because of the large computation time needed. The hybrid models described in the next section are much less computation intensive but are based on simplifying assumptions on electron transport and cannot describe self-consistently the effect of fluctuations. Anomalous electron transport is taken into account in these models by considering a classical expression of the electron mobility and diffusion, but using an 'effective' collision frequency including the effects of electron–atom collisions ν_a, Coulomb collisions ν_C electron–wall collisions ν_w and Bohm-like transport ν_B. Therefore we write: $\nu_m \equiv \nu_{eff} = \nu_a + \nu_C + \nu_w + \nu_B$.

We will see in the next section that the PIC simulations as well as LIF measurements suggest that the anomalous electron mobility associated with ν_w and ν_B can actually not be described by simple $1/B_r^2$ or $1/B_r$ laws.

3. PIC and hybrid models and comparisons with experiments

The 2D PIC model developed by Adam *et al* [17] is two dimensional, in the axial and the azimuthal directions. The geometry is actually further simplified by using a Cartesian simulation domain, the azimuthal direction being represented by the direction y perpendicular to E and B (which is a good approximation for large enough channel radii). In spite of this Cartesian domain, we will continue to use the word 'azimuthal' to characterize the y direction. The model does not resolve the radial direction, and the plasma properties are calculated as a function of (x, y).

In order to reduce the computational cost, periodic boundary conditions are used in the y direction, with a total simulated length in this direction much smaller than $2\pi R$ where R is the mean channel radius. The length of the simulation domain in the x direction is 4 cm, shorter than in the hybrid simulations of figure 2, to reduce computational costs. The PIC model is implicit [17], which allows to overcome the time step limitation related to the plasma frequency, but the electron cyclotron frequency must be resolved. The applied magnetic field is purely radial (perpendicular to x, y) and its dependence on x is given.

Figure 3(*b*) shows the calculated time averaged axial electric field and the rms value of the electric field for an applied potential of 300 V together with the applied radial magnetic field (figure 3(*a*)).

Figure 4 displays pseudocolour maps of the axial and the azimuthal components of the electric field. In figure 4(*a*) we have suppressed the average value along the y direction of the axial electric field E_x in order to make fluctuations visible. Figure 4(*b*) corresponds to the azimuthal electric field E_y. We see in this figure strong oscillations of both components of the electric field in the azimuthal direction. This fluctuations are correlated with azimuthal oscillations of the electron density as it should be for an electrostatic model solving the Poisson equation. The source of these fluctuations has been shown to be the cyclotron electron drift instability [33]. It should be noted that their amplitude is fairly large, of the order of 10^4 V m^{-1}, a significant fraction of the axial electric field.

The electron mobility perpendicular to B can also be deduced directly from PIC simulation by calculating the ratio $\mu_\perp \approx j_{ex}/en_eE_x$ as a function of the axial position. This mobility is represented in figure 5 and has been obtained by averaging J_x and E_x along the y direction and over 1 μs. We see in figure 5 that the calculated mobility is on the order of 0.1 m^2 V^{-1} s^{-1} at the minimum, i.e. where the magnetic field is maximum. Close to the anode the mobility

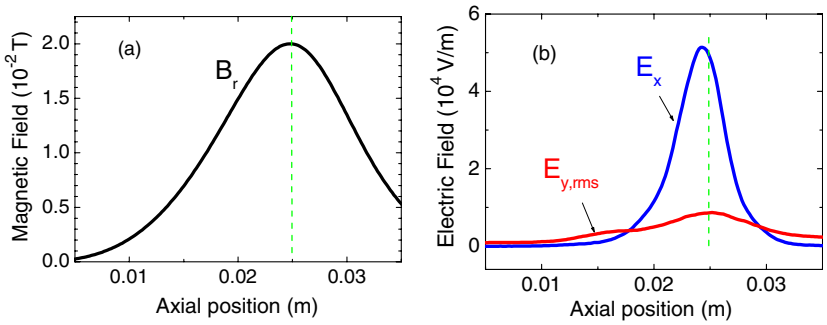

Figure 3. Axial distribution of (*a*) the applied radial magnetic field and (*b*) the calculated time averaged electric field components obtained with the 2D PIC simulation. The mass flow rate is 5 mg s^{-1}, and the applied voltage is 300 V. The length of the simulation domain is 4 cm, the exhaust plane is located near the maximum of the magnetic field, i.e. around $x = 2.5$ cm and is marked as a dashed line.

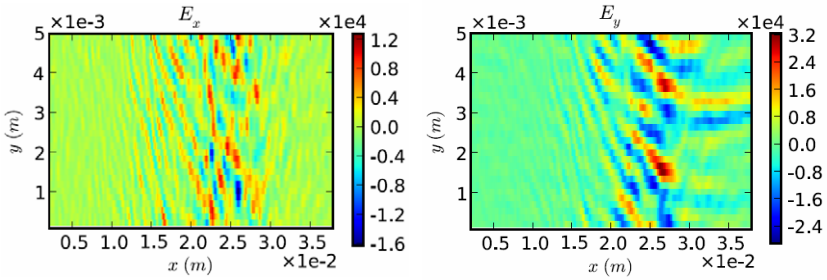

Figure 4. 2D structure of the fluctuating components of the electric field. The color scale is in V m^{-1}.

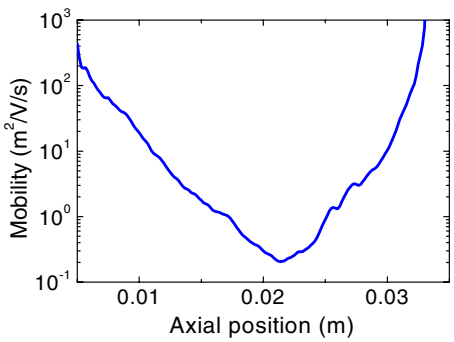

Figure 5. Effective mobility across the magnetic field obtained from the PIC simulations by $\mu_\perp \approx j_{ex}/en_e E_x$, as a function of axial position.

is given by the classical mobility, but outside the channel in the region where electron–atom collisions are negligible it varies with the magnetic field much faster than $1/B$ or $1/B^2$.

It should be pointed out however that this mobility while useful in the hybrid model is a poor representation of the true physics of anomalous conductivity. This is demonstrated in figure 6 which shows two computations of the energy deposition by the Joule effect. Figure 6(*a*) is a fluid approximation based on the preceding evaluation of the mobility while figure 6(*b*) is

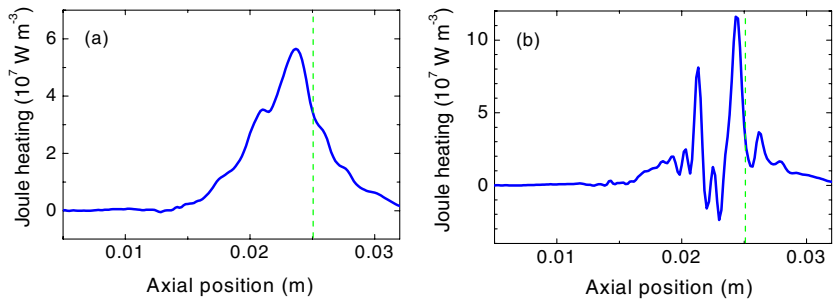

Figure 6. Energy deposition by Joule effect in the PIC code, (*a*) as calculated by the fluid approximation and (*b*) directly obtained from the particles.

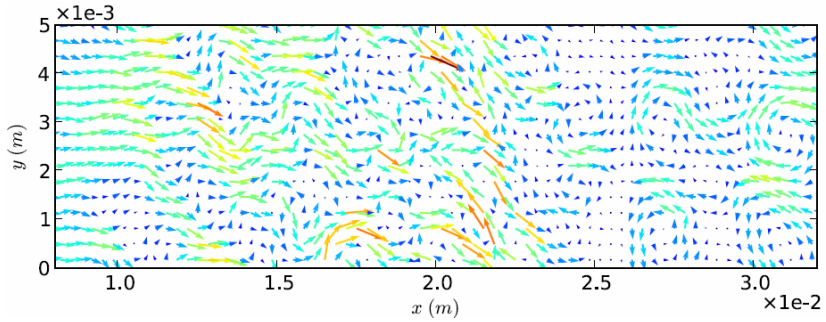

Figure 7. 2D structure of the current as seen in the reference frame rotating at the electron drift velocity.

obtained by computing this term particle by particle in a PIC code.

The observed discrepancy can only be explained by the presence of strong correlations between E and J at the macroscopic level. The complexity of the flow is displayed in figure 7 which shows the structure of the current in the system. For readability the average value of the current density in the y direction has been removed. This is equivalent to a change in reference frame: it is the picture of the current as seen by the electron in the drift velocity frame. Well organized structures can clearly be seen with an average component in the axial direction only clearly visible in the collisional region close to the anode.

The hybrid model is a simpler and much less computationally intensive model that could be used for parametric studies. It is two dimensional in (x, r). Ions and atoms are described kinetically while electrons are described as a fluid. The plasma is supposed to be quasi-neutral and the electric potential distribution is obtained by writing a simplified momentum transfer equation where electrons are in Boltzmann equilibrium along the magnetic field lines. The consequence of this is that the electric potential at a given location can be written as (Morozov assumption)

$$V(x, r) = V^*(\lambda) + \frac{kT_e(\lambda)}{e} \ln \frac{n(x, r)}{n_0}, \tag{3}$$

where V^* is a function, T_e is the electron temperature, n_0 is a reference density and λ a stream function constant along the magnetic field lines. While the electric potential V, and the plasma density n vary over all space, V^* and T_e depend only on the stream function λ. $V^*(\lambda)$ and the potential distribution $V(x, r)$ are obtained by solving the differential equation resulting from

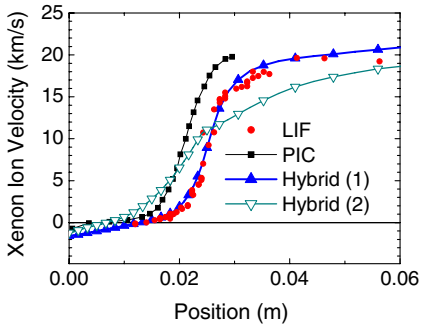

Figure 8. Measured (LIF) and calculated (PIC and hybrid models) xenon ion velocity as a function of axial position (along a line going through the middle of the channel). The conditions for the experiments and the hybrid model are the same as in figure 2. The hybrid model results have been obtained for two different assumptions on the electron mobility (see text and figure 9). The conditions for the PIC simulations are the same as in figure 3, i.e. the simulated domain is shorter for the PIC model (to save computation time). The LIF measurements and PIC simulation results are taken from [21].

the combination of the current continuity equation between two stream lines (the ion current is deduced from the particle description of ion transport) and the electron momentum equation in the direction perpendicular to the magnetic field (drift–diffusion form). The plasma density is deduced from the simulation of ion transport while the electron temperature is obtained from an electron energy equation assuming a Maxwellian distribution. A detailed description of the model can be found in Hagelaar *et al* [18], and Bareilles *et al* [19]. Finally, the neutral atom transport model includes the description of neutral atom injection from the anode, atom collisions with walls, generation of atoms at the walls due to recombination of ions with electrons and atom losses due to ionization.

The hybrid model cannot describe self-consistently anomalous transport, and the mobility perpendicular to the magnetic field in the electron drift–diffusion momentum equation is represented as $\mu_\perp \approx \frac{1}{B_r}\frac{\nu_{\rm eff}}{\Omega}$, where $\nu_{\rm m} \equiv \nu_{\rm eff} = \nu_{\rm a} + \nu_{\rm C} + \nu_{\rm w} + \nu_{\rm B}$ is an effective momentum transfer frequency as discussed in section 2. We have tried in previous papers to represent anomalous transport by a combination of wall effects and Bohm-like transport (e.g. $\nu_{\rm w} = \alpha\nu_{\rm ref}$, $\nu_{\rm B} = K\Omega/16$, as in [7, 18–20], where α and K are adjustable coefficients and $\nu_{\rm ref} = 10^7\ {\rm s}^{-1}$). Although such a representation of anomalous transport was sufficient to reproduce many features and properties of the thruster (current amplitude and oscillation frequency, part of the potential distribution inside and outside the channel, thrusters performance), we recently realized, by using more detailed comparisons with experiments, that this representation is actually not accurate.

Comparisons between the hybrid model results and experimental measurements of the space distribution of the xenon ion velocity (see figure 8) show that it is quite difficult to reproduce a realistic profile of xenon ion velocity along the thruster axis by assuming a $1/B^2$ (or $1/B$) mobility inside the channel and a $1/B$ mobility outside the channel. Reproducing the measured ion velocity profile was possible by adjusting the anomalous mobility as shown in figure 9(*a*) (corresponding to the calculated velocity profile indicated 'hybrid (1)' in figure 8). $1/B^2$ and $1/B$ mobility profiles inside and outside the channel respectively, as shown in figure 9(*b*) (and used in previous work [7, 18, 19]) led to the ion velocity space distribution indicated 'hybrid (2)' in figure 8, very different from the LIF experiments and PIC simulation results.

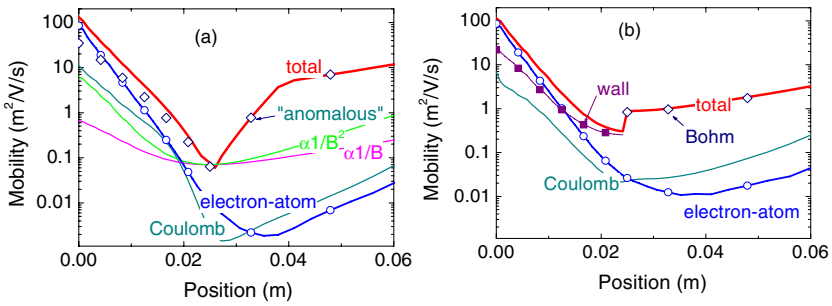

Figure 9. Effective mobility and different contributions to the effective mobility with two different assumptions on the 'anomalous' mobility for the hybrid model results of figure 8; (*a*) hybrid model results indicated (1) in figure 8; (*b*) hybrid model results indicated (2) in figure 8.

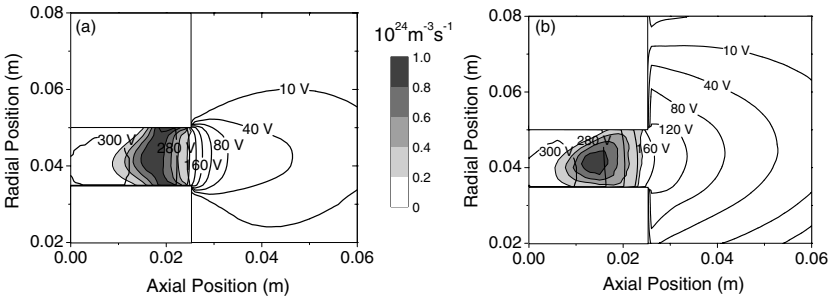

Figure 10. Time averaged electric potential (contours) and ionization rate (grey scale) calculated with the hybrid model in the conditions of figure 2, and for two different assumptions, (*a*), and (*b*), on the 'anomalous' mobility indicated in figures 8(*a*) and (*b*), respectively.

The PIC simulation results of figure 8 (taken from [21]) give a velocity profile in good agreement with the experiments but shifted toward the inside of the channel, probably because of the fact that the extension of the external region of the thruster taken into account in the simulation was short (to limit the computational cost). Note that Koo and Boyd [8] performed similar comparisons between experiments (space resolved probe measurements) and hybrid models for different assumptions on the anomalous mobility. Their conclusions are consistent with results shown in figures 8 and 9.

Finally, we present in figure 10 the calculated, time averaged, electric potential contours and ionization rate distribution in the thrusters for the two anomalous mobility profile used in figure 8 and represented in figure 9. The large difference between the two results illustrates the importance of a good characterization of the anomalous mobility to be able to predict the beam divergence and the channel wall erosion due to ion sputtering.

4. Experimental investigation of the Xe^+ ion transport properties

4.1. Measurements of the ion VDFs

The Xe^+ ion VDF is a useful quantity to be measured in a HET because it can be directly compared with the outcomes of simulations and increase our insight into the physics of the thruster. In this contribution, we report on measurements by LIF spectroscopy of the Xe^+ ion VDF in the plasma of the PPS®X000 HET over a broad range of discharge voltages. The

PPS®X000 is a laboratory model based on the 5 kW class Snecma-built PPS®5000 thruster [22]. During the measurements campaign, the discharge voltage was varied from 300 up to 700 V while the xenon mass flow rate through the anode and the cathode as well as the magnetic field were kept unchanged at 6 mg s^{-1}, 0.5 mg s^{-1} and about 150 G (17 A flowing through the coils), respectively. The non-intrusive LIF spectroscopy technique has been used in the past few years to measure the velocity of metastable Xe^+ ions in the plasma of several Hall thrusters [21, 23–26]. The transition used in this study is the $5d\,^2F_{7/2} \rightarrow 6p\,^2D_{5/2}$ at $\lambda = 834.7233$ nm, which has been chosen due to a large population in the $5d\,^2F_{7/2}$ metastable state of Xe^+ ion and due to the favorable branching ratio of the $\lambda = 541.915$ nm line originating from its upper state. Measuring the frequency at which the laser beam energy is absorbed permits to determine the ion Doppler shift and to subsequently calculate the ion velocity component along the laser beam direction [21].

The LIF optical bench along with the methodology is extensively described in [21, 23]. We here shortly outline the setup. The laser beam used to excite Xe^+ metastable ions is produced by an amplified tunable single-mode external cavity laser diode (MOPA) that can deliver up to 700 mW of power in the near IR spectral domain. The wavelength is accurately measured by means of a calibrated wavemeter whose absolute accuracy is better than 100 MHz. A plane scanning Fabry–Pérot interferometer is used to real-time check the quality of the laser mode and to warrant mode-hop free operation of the laser. The laser beam is modulated by a mechanical chopper at ∼400 Hz before being coupled into a single-mode optical fiber to carry the light into the PIVOINE-2g ground-test facility [22]. Collimation optics are used to form a narrow beam that passes through a hole 2.2 mm in diameter located at the back of the PPS®X000 thruster. The laser beam propagates along the channel axis in the direction of the ion flow. About 3 mW mm^{-2} of power is deposited into the detection volume to limit the saturation effect. Fluorescence collection optics are mounted onto a travel stage perpendicular to the channel axis. A slit 16 mm in length was made in the channel dielectric outer wall in order to carry out measurements inside the channel. The LIF light is transported by a 200 μm fiber toward the entrance slit of a 20 cm focal length monochromator equipped with a PMT. A lock-in amplifier operating at the chopper frequency is used to discriminate the fluorescence light from the intrinsic plasma emission. As explained in previous papers [21, 23], the fluorescence profile images the local Xe^+ ion VDF. Four raw Xe^+ ion axial VDF are shown in figure 11.

4.2. On-axis velocity profile and electric field distribution

The evolution of the Xe^+ ion mean axial velocity component as a function of the axial position x is displayed in figure 12 for a set of discharge voltages, others parameters being kept fixed.

The mean velocity is computed from the first order moments of the VDF. Also shown in figure 12 is the ion velocity obtained assuming a full conversion of the potential energy eU_d. The mean velocity approaches the theoretical limit in the plume near field, which means a large part of the applied potential is converted into ion axial motion [21, 23, 26]. The shape of the velocity profile depends on the applied voltage, see figure 12: the gradient is steeper when U_d is ramped up and the whole profile is shifted toward the anode. A striking feature is the existence of Xe^+ ions with a kinetic energy above eU_d. In figure 12, we also plotted the on-axis profile of the maximum ion velocity v_{max}; this is the velocity for which the amplitude of the distribution drops to 10% of its maximum value on the high velocity side [21, 23]. As can be seen, there is a non negligible fraction of Xe^+ ions with a velocity greater than the theoretical limit. Such very fast ions were also detected by means of mass spectrometer [27] and repulsing potential analyzer [28]. Naturally, to fulfil the energy conservation principle, very slow ions also exist in the discharge of a Hall thruster [21, 23]. PIC and hybrid simulations suggest that

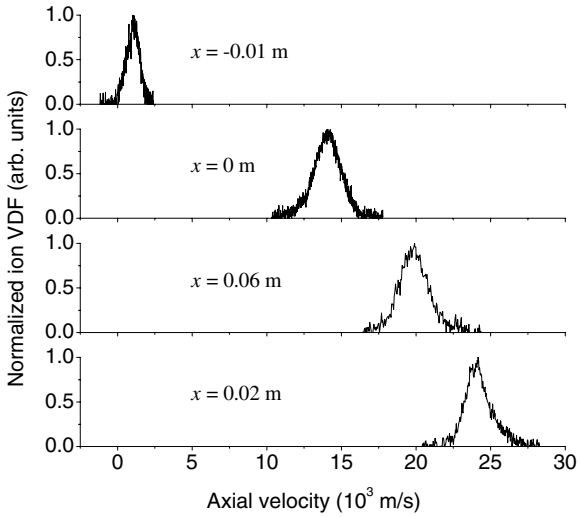

Figure 11. Examples of raw Xe^+ ion VDF obtained by LIF spectroscopy at various positions along the channel axis of the PPS®X000 thruster. The position $x = 0$ mm corresponds to the channel exit plane. The thruster operating conditions are: 500 V applied voltage, 6 mg s^{-1} xenon flow at the anode and 17 A in the coils.

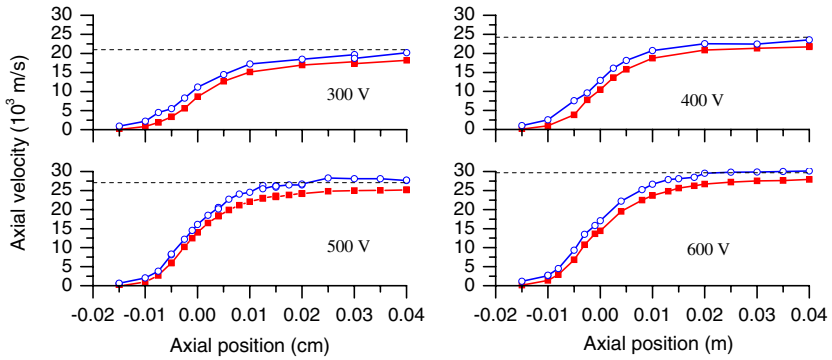

Figure 12. Xe^+ ion axial velocity component as a function of the position x along the channel axis of the PPS®X000 thruster for several values of U_d (6 mg s^{-1}, 17 A). The mean velocity (square) and the maximum velocity (circle) are plotted. The dashed line corresponds to the velocity achieved after full conversion of the potential energy eU_d.

the presence of ions with energy larger than the applied potential is associated with the space and time oscillations of the electric field.

The electric field in the axial direction E_x can be obtained from the measured axial velocity profile [21, 23]. The electric field distribution along the channel axis is shown in figure 13 for various voltages. In this figure, the electric field is calculated from the Xe^+ ions mean velocity profile. As the mean velocity accounts for ions created in the acceleration layer, this approach leads to an underestimated electric field. On the contrary, using the maximum velocity v_{max}, one favors very fast ions and the electric field is overestimated.

A proper way to extract the distribution of E_x is to compute the moments of the Boltzmann equation using the experimental VDFs. This approach is accurately described in [30]. As

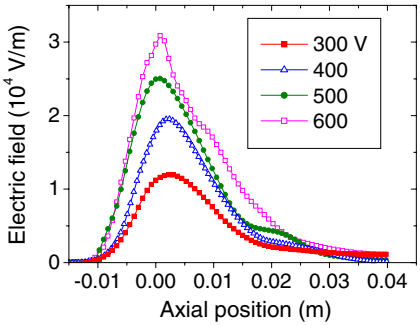

Figure 13. On-axis development of the PPS®X000 thruster acceleration electric field E_x as a function of the applied voltage (6 mg s^{-1}, 17 A). The electric field is computed from the mean ion velocity.

seen in figure 13, when U_d is ramped up the magnitude of E_x increases and the field shifts upstream [23]. A large fraction of the electric field profile of about 60–70% is situated outside the channel whatever the voltage. Moreover, the electric field on-axis distribution seems to spread out when the voltage rises.

5. Diagnostics of the turbulence

The observed electron anomalous transport as well as the predictions of the PIC model point to the role of E-field high frequency and small-scale fluctuations in the thruster plasma. To check the existence and properties of such volume fluctuations, collective light scattering from the expected density irregularities is most appropriate.

5.1. Scattering device

The CS optical bench PRAXIS (PRopulsion Analysis eXperiments via Infrared Scattering) has been specifically built to investigate the thruster plasma. It uses a single-mode CO_2 laser of 42 W continuous power, a sensitive heterodyne detection device, Gaussian profile beam optics with a beam size of $w = 2.5$ mm in the observed region, a scattering angle θ between 8 and 21 mrad. The signal is proportional to the spatial Fourier transform of the electron density fluctuations [30–32] at a wave vector k equal to the difference between the 'scattered' and the 'incident' electromagnetic wave vectors, k_s and k_i, respectively,

$$\vec{k} = \vec{k}_s - \vec{k}_i \tag{4}$$

and

$$\theta = \text{angle}(\vec{k}_i, \vec{k}_s). \tag{5}$$

The primary and scattered beams enter and exit the PIVOINE thruster test chamber through two transparent ZnSe windows that are placed opposite each other, on each side of the thruster axis. Each window is at a distance of 1.2 m from the chamber axis. The small scattering angle allows for the two beams to enter and exit within the constraints of the window diameter. The optical beams cross the thruster axis perpendicularly and at the same height. The observed volume is a cylinder of diameter 2.5 mm and length 250 mm perpendicular to the thruster axis. This volume crosses the annular thruster plasma in two symmetrical regions. The observation wave vector direction $\boldsymbol{k}$ is vertical, corresponding to the direction of the $E \times B$ drift in the annular plasma.

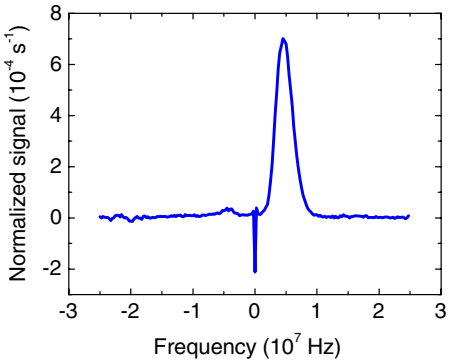

Figure 14. Collective light scattering frequency spectrum in the thruster plasma. k is along the $E \times B$ drift; the frequency analysis is performed from −25 to +25 MHz, over a large number of repeated sequences of 200 consecutive data obtained at a rate of 50 MHz. The plasma signal spectrum is obtained as a difference between the total (plasma-plus-background) spectrum and the background spectrum. The line frequency is of the order of that of an ion acoustic wave.

5.2. Signal processing and spectra

The photocurrent which issues from the detector is amplified in a low noise pre-amplifier and demodulated into its real and imaginary parts by the second, analogous stage of the heterodyne detection. These two parts are simultaneously recorded at a rate of 50 MHz into two memory buffers each of 6.5 Mega-samples. The samples are transferred to a laptop computer. A complex Fourier spectral analysis of these signals is performed. The weak scattered signal spectral density is extracted by repeating the signal frequency analysis a large number of times. The plasma scattered part is obtained as the difference between this spectral density and the spectral density obtained by a similar long recording but with the plasma off. This way a plasma signal amplitude as small as 1/100 of the background photon noise can be appreciated.

An example of a plasma scattered frequency spectrum is shown in figure 14. It is calibrated in units of 'seconds' as the 'dynamic form factor' $S(k, \omega)$ by using the known optical bench and plasma parameters [31, 32]. Its integral over frequencies provides the dimensionless 'form factor',

$$S(k) = \int \frac{\mathrm{d}\omega}{2\pi} S(k, \omega). \tag{6}$$

5.3. Fluctuations propagating along $E \times B$

The spectrum in figure 14 shows a well-defined peak at a frequency of about 4.5 MHz, and a less intense symmetric band at −4.5 MHz. The wave vector is vertical, and the wave number k is 9630 rad m^{-1}. The scattering volume is at a distance of 7.5 mm from the thruster output plane. The optical sensitivity in the observation volume is non-uniform, varying as a Gaussian as the position is moved from the center of the volume. The volume center is not on the thruster axis, but about 15–20 cm before it, at the same vertical level. Thus the observed fluctuations are situated on one side of the plasma ring. On this observed side, the $E \times B$ drift is upward and parallel to the wave vector. The positive line frequency means a phase velocity pointing in the same direction as $E \times B$.

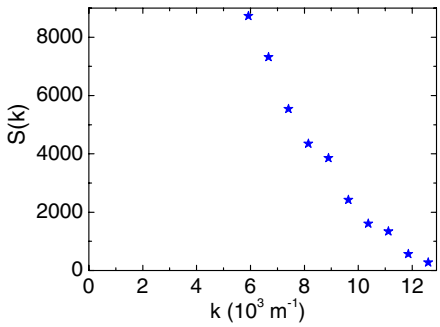

Figure 15. Variation as a function of k of the form factor for fluctuations propagating along the $E \times B$ drift.

The plasma is situated in a magnetic field of 15 mT, the extracting E-field is about 10 kV m^{-1}. The corresponding drift velocity E/B is 6.7×10^5 m s^{-1}. The drift-cyclotron wave number $k_D = \Omega V_D$ is 3960 rad m^{-1}, thus $kV_D/\Omega = 2.4$. The observed wavelengths are of the order of, or smaller than, the drift-cyclotron wavelength.

The same kind of single line spectrum as in figure 14 has been observed at different wave numbers. The ratio of the angular frequency to the wave number shows a phase velocity of 3.5×10^3 m s^{-1}. This is much smaller than the ExB drift velocity. Although ion acoustic waves are not expected to propagate in this cross-B direction, the phase velocity lies in the range of that of an ion acoustic wave in a 16 eV electron temperature plasma.

The direction of the analyzing k vector has been changed, from the $E \times B$ direction to that of the thruster (and ion beam) direction. The most intense fluctuations are seen in the $E \times B$ direction.

5.4. Form factor

In order to look at the amplitude of these fluctuations and their variation with scale, the frequency spectrum was integrated over the main peak to obtain the form factor. This was done for different wave numbers, the k vector being kept parallel to the $E \times B$ drift. The result is shown in figure 15. The fluctuation intensity is large. The form factor is measured (under an assumed electron density of 10^{18} m^{-3}) at a factor 10^4 above the thermal noise at large scales, then it decays almost linearly in the observed range. No periodicity can be observed; the characteristic wave number increment over which the form factor decays by a factor 2 is 3000 rad m^{-1}.

The same data as in figure 15 were plotted on log–log scales. Unlike for turbulent fluctuations, this does not show a unique power index variation.

The form factor intensity is maximum near the thruster and decays as the distance between the thruster front plane and the observation region is increased.

5.5. Observed fluctuation and their expectations

The fluctuations observed by CS show interesting similarities with, and deviation from, expectations.

A linear theory of the fluctuations in a Hall thruster was presented in Adam *et al* [17] (see also Ducroq *et al* [33]). Unstable branches of the dispersion relation were found near discrete values of the perpendicular wave number k, each corresponding to an integer value of k/k_D.

For each of these k-values, the unstable frequencies were expected in the 1–10 MHz range, with a very large group velocity.

This is indeed the observed frequency range, except the observed spectrum is made of a single line at a well-defined frequency. As for variation with k, in figure 15 the parameter k/k_D was varied from 1.2 to 3.1 and does not show a discrete behavior. The expected k-periodicity may be smoothed by the k-resolution Δk of the scattering device, since Δk is 1.14×10^3 (FWHM), such that $\Delta k/k_D \approx 0.3$. As for electron transport, the fluctuation amplitude spatial distribution obtained is comparable to that of the expected anomalous electron mobility region required by the hybrid model (figure 8(*a*)).

Fluctuations in the range predicted by the PIC codes with a behavior that is close to the expected anomalous transport have thus been observed by CS. Further observations for different wave numbers and directions will likely provide a more precise picture of the electron transport.

6. Conclusions

The scaling and optimization of HETs requires detailed and accurate modeling. Modeling can help in designing the magnetic field distribution that controls the divergence of the ion beam in the exhaust region and thus the efficiency and lifetime of the thruster.

Hybrid and PIC models and LIF and CS experiments have been combined to improve our insight into the physics of a HET, especially anomalous electron transport. Results show that the LIF measured ion velocity distribution can be reproduced in hybrid models using anomalous transport coefficients that are consistent with PIC model predictions. The anomalous mobility cannot be fitted by $1/B^2$ or $1/B$ laws.

We have also presented in this paper the first direct experimental evidence (using CS measurements of the electron density fluctuations) of the azimuthal drift instability predicted by PIC simulations that contributes to anomalous electron transport in the thruster. This is a very promising result and more work will be devoted in the future to a better understanding, characterization and scaling of this instability.

Acknowledgments

The work presented in this paper has been performed in the frame of the TELIOPEH (‘*Transport ELectronique et IOnique dans les Propulseurs à Effet Hall*’) project, funded by ANR (National Research Agency), under contract ANR-06-BLAN-0171. The authors would like to acknowledge the support from the Joint Research Program 3161 CNRS/CNES/SNECMA/Universités ‘*Propulsion Spatiale à Plasma*’.

References

[1] Saccoccia G, Gonzalez del Amo J and Estublier D 2001 Electric propulsion: a key technology for space missions in the new millennium *esa Bulletin* 101
[2] Jahn R G and Choueiri Y 2005 Electric propulsion *Encyclopedia of Science and Technology* 3rd edn **5** 125
[3] Bouchoule A, Cadiou A, Heron A, Dudeck M and Lyszyk M 2001 An overview of the French research program on plasma thrusters for space applications *Contrib. Plasma Phys.* **41** 57
[4] Morozov A I 2003 The conceptual development of stationary plasma thrusters *Plasma Phys. Rep.* **29** 235
[5] Morozov A I and Savelyev V V 2000 Fundamentals of stationary plasma thruster theory *Reviews of Plasma Physics* vol 21 ed B B Kadomstev and V D Shafranov (Dordecht: Kluwer)
[6] Kim V 1998 Main physical features and processes determining the performance of stationary plasma thrusters *J. Propulsion Power* **14** 736

[7] Boeuf J P and Garrigues L 1998 Low frequency oscillation in a stationary plasma thruster *J. Appl. Phys.* **84** 3541
[8] Koo J W and Boyd I D 2006 Modeling of anomalous electron mobility in Hall thrusters *Phys. Plasmas* **13** 033501
[9] Janes G S and Lowder R S 1966 Anomalous electron diffusion and ion acceleration in a low density plasma *Phys. Fluids* **9** 1115
[10] Haas J M and Gallimore A D 2001 Internal plasma potential profiles in a laboratory-model Hall thruster *Phys. Plasmas* **8** 652
[11] Meezan N B, Hargus W A Jr and Cappelli M A 2001 Anomalous electron mobility in a coaxial Hal discharge plasma *Phys. Rev.* E **63** 026410
[12] Scharfe M K, Gascon N and Cappelli M A 2006 Comparisons of hybrid Hall thrusters model to experimental measurements *Phys. Plasmas* **13** 083505
[13] Ahedo E, Gallardo J M and Martınez-Sanchez M 2003 Effects of the radial plasma–wall interaction on the Hall thruster discharge *Phys. Plasmas* **10** 3397
[14] Barral S, Makowski K, Peradynski Z, Gascon N and Dudeck M 2003 Wall material effects in stationary plasma thrusters *Phys. Plasmas* **10** 4137
[15] Garrigues L, Hagelaar G J M, Boniface C and Boeuf J P 2006 Anomalous conductivity and secondary emission in Hall effect thrusters *J. Appl. Phys.* **100** 123301
[16] Sydorenko D, Smolyakov A, Kaganovich I and Raitses Y 2006 Kinetic simulation of secondary electron emission effects in Hall thrusters *Phys. Plasmas* **13** 014501
[17] Adam J C, Heron A and Laval G 2004 Study of stationary plasma thrusters using two-dimensional fully kinetic simulations *Phys. Plasmas* **11** 295
[18] Hagelaar G J M, Bareilles J, Garrigues L and Boeuf J P 2002 Role of anomalous electron transport in a stationary plasma thruster simulation *J. Appl. Phys.* **93** 67
[19] Bareilles J, Hagelaar G J M, Garrigues L, Boniface C, Boeuf J P and Gascon N 2004 Critical assessment of a two-dimensional hybrid Hall thruster model: comparisons with experiments *Phys. Plasmas* **11** 3035
[20] Boniface C, Garrigues L, Hagelaar G J M and Boeuf J P 2006 Anomalous cross field electron transport in a Hall effect thrusters *App. Phys. Lett.* **89** 161503
[21] Gawron D, Mazouffre S, Sadeghi N and Héron A 2008 Influence of magnetic field and discharge voltage on the acceleration layer features in a Hall effect thruster *Plasma Sources Sci. Technol.* **17** 025001
[22] Mazouffre S, Lazurenko A, Lasgorceix P, Dudeck M, d'Escrivan S and Duchemin O 2007 Expanding frontiers: towards high power Hall effect thrusters for interplanetary journeys *Proc. 7th Int. Symp. on Launcher Technologies (Barcelona, Spain)* paper O-25
[23] Mazouffre S, Gawron D, Kulaev V and Sadeghi N 2008 Xe+ ion transport in the crossed-field discharge of a 5 kW-class Hall effect thruster *IEEE Trans. Plasma Sci.* at press
[24] Hargus W A and Cappelli M A 2001 Laser-induced fluorescence measurements of velocity within a Hall discharge *Appl. Phys.* B **72** 961
[25] Dorval N, Bonnet J, Marque J P, Rosencher E, Chable S, Rogier F and Lasgorceix P 2002 Determination of the ionization and acceleration zones in a stationary plasma thruster by optical spectroscopy study: experiments and model *J. Appl. Phys.* **91** 4811
[26] Hargus W A and Charles C S 2008 Near exit plane velocity field of a 200-Watt Hall thruster *J. Propulsion Power* **24** 127
[27] King L B and Gallimore A D 2004 Ion-energy diagnostics in an SPT-100 plume from thrust axis to backflow *J. Propulsion Power* **20** 228
[28] King L B, Gallimore A D and Marrese C M 1998 Transport-property measurements in the plume of an SPT-100 Hall thruster *J. Propulsion Power* **14** 327
[29] Pérez-Luna J, Hagelaar G J M, Garrigues L and Boeuf J P 2008 Means of investigation of laser induced fluorescence measurements in low-pressure plasmas *Plasma Sources Sci. Technol.* at press
[30] Grésillon D M and Honoré C 1994, Collective light scattering: an introduction *Optical Diagnostics for Flow Processes* ed L Lading *et al* (New York: Plenum) pp 229–43
[31] Holzhauer E and Massig J H 1978 An analysis of optical mixing in plasma scattering experiments *Plasma Phys.* **20** 867–77
[32] Grésillon D, Stern C, Hémon A, Truc A, Lehner T, Olivain J, Quémeneur A, Gervais F and Lapierre Y 1982 Density fluctuation measurement by far infrared light scattering *Phys. Scr.* **T2:2** 459–66
[33] Ducrocq A, Adam J C, Héron A and Laval G 2006 High-frequency electron drift instability in the cross-field configuration of Hall thrusters *Phys. Plasmas* **13** 102111